



# *In situ* high-resolution thermal microscopy on integrated circuits

GUAN-YU ZHUO,<sup>1</sup> HAI-CHING SU,<sup>2</sup> HSIEN-YI WANG,<sup>3,4</sup> AND MING-CHE CHAN<sup>5,\*</sup>

<sup>1</sup>*Institute of Medical Science and Technology, National Sun Yat-sen University, No. 70, Lienhai Rd., Kaohsiung 80424, Taiwan*

<sup>2</sup>*Institute of Lighting and Energy Photonics, College of Photonics, National Chiao-Tung University, No. 301, Gaofa 3rd Rd., Guiren Dist., Tainan City 71150, Taiwan*

<sup>3</sup>*Department of Sports Management, College of Leisure and Recreation Management, Chia Nan University of Pharmacy and Science, Rende District, Tainan, Taiwan*

<sup>4</sup>*Department of Nephrology, Chi-Mei Medical Center, Tainan, Taiwan*

<sup>5</sup>*Institute of Photonic System, College of Photonics, National Chiao-Tung University, No. 301, Gaofa 3rd Rd., Guiren Dist., Tainan City 71150, Taiwan*

\*[mcchan@nctu.edu.tw](mailto:mcchan@nctu.edu.tw)

**Abstract:** The miniaturization of metal tracks in integrated circuits (ICs) can cause abnormal heat dissipation, resulting in electrostatic discharge, overvoltage breakdown, and other unwanted issues. Unfortunately, locating areas of abnormal heat dissipation is limited either by the spatial resolution or imaging acquisition speed of current thermal analytical techniques. A rapid, non-contact approach to the thermal imaging of ICs with sub- $\mu\text{m}$  resolution could help to alleviate this issue. In this work, based on the intensity of the temperature-dependent two-photon fluorescence (TPF) of Rhodamine 6G (R6G) material, we developed a novel fast and non-invasive thermal microscopy with a sub- $\mu\text{m}$  resolution. Its application to the location of hotspots that may evolve into thermally induced defects in ICs was also demonstrated. To the best of our knowledge, this is the first study to present high-resolution 2D thermal microscopic images of ICs, showing the generation, propagation, and distribution of heat during its operation. According to the demonstrated results, this scheme has considerable potential for future *in situ* hotspot analysis during the optimization stage of IC development.

© 2017 Optical Society of America

**OCIS codes:** (000.6850) Thermodynamics; (000.4930) Other topics of general interest; (110.6820) Thermal imaging; (350.5340) Photothermal effects; (000.2170) Equipment and techniques.

## References and links

1. G. E. Moore, "Cramming more components onto integrated circuits," *Electronics (Basel)* **38**(8), 114–117 (1965).
2. G. E. Moore, "Progress in Digital Integrated Electronics," in *Technical. Digest of International Electron Devices Meeting (IEEE, 1975)*, pp. 11–13.
3. M. Ashauer, J. Ende, H. Glosch, H. Haffner, and K. Hiltmann, "Thermal characterization of micro systems by means of high-resolution thermography," *Microelectronics J.* **28**(3), 327–335 (1997).
4. J. Kölzer, A. Dallmann, G. Deboy, J. Otto, and D. Weinmann, "Emission microscopy," *Qual. Reliab. Eng. Int.* **8**(3), 225–237 (1992).
5. K. Nikawa, S. Inoue, K. Morimoto, and S. Sone, "Failure analysis case studies using the IR-OBIRCH (infrared optical beam induced resistance change) method," in *Proceedings of the 8th Asian Test Symposium (IEEE Computer Society, 1999)*, pp. 394–399.
6. K. Nikawa, C. Matsumoto, and S. Inoue, "Novel method for defect detection in Al stripes by means of laser beam heating and detection of changes in electrical resistance," *Jpn. J. Appl. Phys.* **34**(1), 2260–2265 (1995).
7. G. Tessier, M. Bardoux, C. Filloy, C. Boué, and D. Fournier, "High resolution thermal imaging inside integrated circuits," *Sens. Rev.* **27**(4), 291–297 (2007).
8. A. Csendes, V. Székely, and M. Rencz, "Thermal mapping with liquid crystal method, *Microelectronic Engineering*," *Microelectron. Eng.* **31**(1–4), 281–290 (1996).
9. G. Aszodi, J. Szabon, I. Janossy, and V. Szekely, "High-resolution thermal imaging of microcircuits using nematic liquid crystals," *Solid-State Electron.* **24**(12), 1227–1233 (1981).
10. A. Mandelis, *Photoacoustic and Thermal Wave Phenomena in Semiconductors* (Elsevier Amsterdam, 1st ed., New York, 1987).

11. E. Hernández-Rosales, E. Cedeño, J. Hernandez-Wong, J. B. Rojas-Trigos, E. Marin, F. C. G. Gandra, and A. M. Mansanares, "Thermoacoustic and thermoreflectance imaging of biased integrated circuits: voltage and temperature maps," *Appl. Phys. Lett.* **109**(4), 041902 (2016).
12. W. Jeong, K. Kim, Y. Kim, W. Lee, and P. Reddy, "Characterization of nanoscale temperature fields during electromigration of nanowires," *Sci. Rep.* **4**(1), 4975 (2014).
13. G. Binnig, H. Rohrer, C. Gerber, and E. Weibel, "Surface studies by scanning tunneling microscopy," *Phys. Rev. Lett.* **49**(1), 57–61 (1982).
14. K. Kim, J. Chung, G. Hwang, O. Kwon, and J. S. Lee, "Quantitative measurement with scanning thermal microscope by preventing the distortion due to the heat transfer through the air," *ACS Nano* **5**(11), 8700–8709 (2011).
15. F. Menges, P. Mensch, H. Schmid, H. Riel, A. Stemmer, and B. Gotsmann, "Temperature mapping of operating nanoscale devices by scanning probe thermometry," *Nat. Commun.* **7**, 10874 (2016).
16. S. Yatsyshyn, *Handbook of Thermometry and Nanothermometry* (International Frequency Sensor Association Publishing, Spain, 2015).
17. R. Heiderhoff, A. Makris, and T. Riedl, "Thermal microscopy of electronic materials," *Mater. Sci. Semicond. Process.* **43**, 163–176 (2016).
18. L. Salmon, G. Molnar, D. Zitouni, C. Quintero, C. Bergaud, J. C. Micheau, and A. Bousseksou, "A novel approach for fluorescent thermometry and thermal imaging purposes using spin crossover nanoparticles," *J. Mater. Chem.* **20**(26), 5499–5503 (2010).
19. L. M. Maestro, E. M. Rodríguez, F. S. Rodríguez, I. Cruz, A. Juarraz, R. Naccache, F. Vetrone, D. Jaque, J. A. Capobianco, and J. G. Sole, "CdSe Quantum Dots for Two-Photon Fluorescence Thermal Imaging," *Nano Lett.* **10**(12), 5109–5115 (2010).
20. A. Benayas, E. Escuder, and D. Jaque, "High-resolution confocal fluorescence thermal imaging of tightly pumped microchip Nd:YAG laser ceramics," *Appl. Phys. B* **107**(3), 697–701 (2012).
21. R. F. Kubin and A. N. Fletcher, "Fluorescence quantum yields of some rhodamine dyes," *J. Lumin.* **27**(4), 455–462 (1982).
22. K. Kolmakov, V. N. Belov, J. Bierwagen, C. Ringemann, V. Müller, C. Eggeling, and S. W. Hell, "Red-Emitting Rhodamine Dyes for Fluorescence Microscopy and Nanoscopy," *Chemistry* **16**(1), 158–166 (2010).
23. J. Arden, G. Deltau, V. Huth, U. Kringel, D. Peros, and K. H. Drexhage, "Fluorescence and lasing properties of rhodamine dyes," *J. Lumin.* **48**, 352–358 (1991).
24. S. Liu, T. P. Lin, D. Li, L. Leamer, H. Shan, Z. Li, F. P. Gabbaï, and P. S. Conti, "Lewis Acid-Assisted Isotopic F-18-F-19 Exchange in BODIPY Dyes: Facile Generation of Positron Emission Tomography/Fluorescence Dual Modality Agents for Tumor Imaging," *Theranostics* **3**(3), 181–189 (2013).
25. M. C. Chan, C. H. Lien, J. Y. Lu, and B. H. Lyu, "High power NIR fiber-optic femtosecond Cherenkov radiation and its application on nonlinear light microscopy," *Opt. Express* **22**(8), 9498–9507 (2014).
26. K. C. Li, L. L. Huang, J. H. Liang, and M. C. Chan, "Simple approach to three-color two-photon microscopy by a fiber-optic wavelength convertor," *Biomed. Opt. Express* **7**(11), 4803–4815 (2016).
27. G. Chirico, F. Cannone, G. Baldini, and A. Diaspro, "Two-photon thermal bleaching of single fluorescent molecules," *Biophys. J.* **84**(1), 588–598 (2003).
28. G. Katona, G. Szalay, P. Maák, A. Kaszás, M. Veress, D. Hillier, B. Chiovini, E. S. Vizi, B. Roska, and B. Rózsa, "Fast two-photon in vivo imaging with three-dimensional random-access scanning in large tissue volumes," *Nat. Methods* **9**(2), 201–208 (2012).
29. E. P. Perillo, J. E. McCracken, D. C. Fernée, J. R. Goldak, F. A. Medina, D. R. Miller, H. C. Yeh, and A. K. Dunn, "Deep in vivo two-photon microscopy with a low cost custom built mode-locked 1060 nm fiber laser," *Biomed. Opt. Express* **7**(2), 324–334 (2016).
30. T. Wang, D. Halaney, D. Ho, M. D. Feldman, and T. E. Milner, "Two-photon luminescence properties of gold nanorods," *Biomed. Opt. Express* **4**(4), 584–595 (2013).
31. B. A. Flusberg, E. D. Cocker, W. Piyawattanametha, J. C. Jung, E. L. M. Cheung, and M. J. Schnitzer, "Fiber-optic fluorescence imaging," *Nat. Methods* **2**(12), 941–950 (2005).
32. M. C. Chan, S. W. Chu, C. H. Tseng, Y. C. Wen, Y. H. Chen, G. D. Su, and C. K. Sun, "Cr:Forsterite-laser-based fiber-optic nonlinear endoscope with higher efficiencies," *Microsc. Res. Tech.* **71**(8), 559–563 (2008).
33. S. H. Chia, C. H. Yu, C. H. Lin, N. C. Cheng, T. M. Liu, M. C. Chan, I. H. Chen, and C. K. Sun, "Miniaturized video-rate epi-third-harmonic-generation fiber-microscope," *Opt. Express* **18**(16), 17382–17391 (2010).
34. T. M. Liu, M. C. Chan, I. H. Chen, S. H. Chia, and C. K. Sun, "Miniaturized multiphoton microscope with a 24Hz frame-rate," *Opt. Express* **16**(14), 10501–10506 (2008).

## 1. Introduction

Moore's law states that the number of transistors in a chip and the chip's operating speed will double approximately every twenty-four months [1, 2]. Exponential growth in the transistor densities and operating frequencies of IC chips has dramatically increased transistor densities as well as the effective current density of chips,  $J$ . The shrinkage of metal wires also increases the effective resistance,  $R$ . The total heat generated in the chip, which is proportional to  $J^2R$ , can melt metal wires and cause open or shorted wires. These open or shorted wires can

themselves introduce unwanted heat within a chip, rendering the overall electronic system unstable and unreliable. Thus, the issue of thermal management is a key factor limiting circuit performance. The locations of breakdowns or weak points (called defects) must be monitored *in situ* during the manufacturing and packaging of ICs.

Infrared (IR) thermography [3, 4] is the simplest optical method for observing the distribution of temperature in ICs. This method uses an IR camera operating at wavelengths of 3-5  $\mu\text{m}$ , based on blackbody radiation. Unfortunately, the diffraction limit of the working wavelength limits the spatial resolution to several  $\mu\text{m}$ . Furthermore, the contrast mechanism of IR thermography does not allow for the imaging of depth.

Several optical as well as non-optical methods have been developed for the detection of defects/hotspots in ICs. Optical methods include optical beam induced resistance change (OBIRCH) [5, 6], NIR thermorefectance [7], and liquid crystal method (LCM) [8, 9]. In OBIRCH, the defects are detected via scanning a laser beam on the IC surface. A portion of photons' energy from the scanned laser beam is absorbed by the metal tracks. The absorbed energy is then transformed into the heat, thereby increasing local temperature. The defects in the metal wires will result in the change of ohmic resistance,  $\Delta R$ . By measuring and analyzing  $\Delta R$  in different positions of ICs, the locations of defects can thus be founded. The contrast mechanism of NIR thermorefectance imaging is based on changes in light reflectance. When changes in the reflectivity of the material  $\Delta r$  are correlated with local changes in temperature  $\Delta T$  (given by  $\Delta r/r = (1/r)(\partial r/\partial T)\Delta T = C\Delta T$ , where  $C$  is the thermorefectance coefficient), the defect point produces an abnormal change in reflectance. Changes in the reflectance of each pixel are then converted into changes in intensity and registered on an image. Furthermore, the analysis of the thermal-wave properties under laser heating can provide additional information about electron-phonon energy relaxation, heat transport properties, and the temperature distribution of electron and phonon [10]. More recently, the thermorefectance imaging is further combined with a lead zirconate titanate (PZT) sensor for thermoacoustic detection in revealing the track structure and voltage distribution. This integrated setup is regarded as a complimentary tool for traditional thermorefectance imaging that only allows the map of current flow [11]. The liquid crystal method (LCM) is highly effective in characterizing thermal flow when an LC kit is deposited on the surface of an IC, due to the fact that the optical properties of LC are highly susceptible to changes in local temperature. Changes in temperature on ICs are converted into dark areas in images, to be revealed using a polarized light microscope where the hotspots make the LC transparent.

OBIRCH and NIR thermorefectance imaging provide sub- $\mu\text{m}$  spatial resolution, which is superior to that of LCM and infrared thermography (spatial resolution of tens of  $\mu\text{m}$ ). OBIRCH and NIR thermorefectance imaging are well-suited to imaging thinner metal tracks; however, the thermal properties of ICs are respectively converted into changes in current  $\Delta i$  or material reflectivity  $\Delta r$ , which are then converted into changes in the intensity of each pixel. This two-step conversion process is indirect and tends to introduce errors, while increasing computation time. Furthermore, these methods are ill-suited to depth imaging with precise optical sectioning, thereby precluding their application to *in situ* temperature imaging deep within ICs.

Non-optical methods, such as scanning probe microscopy (SPM) [12–14], contact the surface of samples through a probe, including a thermocouple, resistance thermometer, magnetic thermometer, or an acoustic resonant thermometer. Scanning the probes makes it possible to produce thermal images with resolutions of several tens of nanometer. Unfortunately, SPM-based thermal imaging is time-consuming (~1 hour imaging time), and therefore prevents the monitoring of thermal-non-equilibrium processes, including the generation, propagation, and diffusion of heat. Furthermore, contact with the sample can cause contact-related artifacts and/or changes in local temperature through thermal conduction. It is unlikely that non-optical methods could ever be used for depth imaging.

Menges et al. recently reported on imaging nano-scale hotspots using an advanced scanning thermal microscope [15]. They reported sub-10 nm spatial resolution and 7 mK temperature resolution at the metal-semiconductor contacts with an indium arsenide nanowire. However, the temperature of the sample must be modulated externally at a particular frequency, which greatly limits the range of applicability. Furthermore, this method is inapplicable to depth imaging.

Addressing the thermal-related issues of ICs requires an accurate, non-contact thermal imaging method with sub- $\mu\text{m}$  spatial resolution and a short imaging acquisition time [16, 17]. In this work, we propose a novel approach to the thermal imaging of ICs based on the temperature-dependent two-photon fluorescence (TPF) intensity of selected materials [18–20]. TPF is the process that two photons with the same wavelength are simultaneously absorbed to excite a fluorescent molecule from ground state to an excited state. Through radiative relaxation, it emits a photon with the energy equivalent to the difference between the involved lower and upper states. The proposed method provides spatial resolution of 0.85  $\mu\text{m}$ , temporal resolution of  $\sim 2$  sec, and temperature precision of less than one degree. The temperature-dependence of fluorescent dyes is used as an intermediate contrast agent to indicate thermal anomalies. In other words, local temperatures are converted directly into TPF intensity values; i.e., single-step conversion. In experiments, we measured the linear relationship between temperature change ( $\Delta T$ ), and changes in TPF intensity ( $\Delta I$ ), as a calibration curve in determining local temperature. We used an IC chip capped with a thin-film of fluorescent dye above the circuit layer as an example for sub-micron thermal imaging. This enables the measurement of temperature in a steady state as well as the dynamic monitoring of the generation, diffusion, and propagation of heat. Analyzing time-lapse TPF thermal images makes it possible to diagnose hotspots or weak structures in circuits at the sub- $\mu\text{m}$  scale. The proposed scheme provides sub-micron resolution, short image acquisition time, high temperature accuracy, easy implementation, simple temperature-to-image conversion, and intrinsic optical sectioning for depth imaging. This method has considerable promise for locating potential defects/hotspots via *in situ* monitoring during IC manufacturing or prior to mass-production.

## 2. Experimental Setup

In our experiment, the setup in Fig. 1 was divided into two parts: (a) and (b). In Part (a), we measured the temperature-dependent TPF intensity and TPF emission spectrum of the fluorescent dyes. Rhodamine 6G (R6G) was selected as the tracer dye because of its high quantum yield (0.95), high photo-stability, high availability, and cost-effectiveness [21]. R6G is widely used in biological applications, such as fluorescence imaging and single molecule detection [21–24]. The thin-film on ICs was spin-coated from Poly(methyl methacrylate) (PMMA) mixed with R6G in chlorobenzene solution. PMMA is a transparent host matrix to disperse R6G molecules and thus a nearly uniform film can be achieved. The temperature of the resistor was determined with a high degree of precision at each time point by an infrared thermometer. While heating the cement resistor, we recorded the TPF signals produced by focused NIR femtosecond pulses using a spectrometer (HR2000 + , Ocean Optics) at various temperatures. The pump source was an air-cooled, ultra-compact, mode-locked Ytterbium fiber laser (Mikan, Amplitude Systems). Typically, it emitted 250 fs pulses at a 1030 nm central wavelength with a 54.77 MHz repetition rate and a 1W average output power [25, 26].

In Part (b), we investigated a R6G-coated IC chip powered by an external  $\pm 15\text{V}$  voltage source under a laser scanning microscope to enable thermal imaging. Image data was then compared with the measurement results from Part (a). The thermal microscope in Fig. 1 is similar to a TPF microscope, comprising a pair of galvano mirrors, a pair of relay lenses, an air microscope objective with 0.9 numerical aperture, a dichroic mirror, and a photomultiplier tube (PMT). The angle of the galvano mirrors could be adjusted to enable the sequential scanning of the IC surface using focused 1.03  $\mu\text{m}$  laser beams with  $\sim 20$  mW laser power. The

typical value of field of view (FOV) and frame-rate in the TPF imaging were  $200\ \mu\text{m}$  by  $200\ \mu\text{m}$  and 0.4-0.5 frames per second (fps), respectively. The generated TPF signals (the intensity of which depends on localized temperature) were reflected and extracted by a dichroic beam splitter for detection using a PMT (R928P, Hamamatsu, Japan). A colored glass filter (KG5, Schott Glass) was placed in front of the PMT to remove background fundamental radiation. The CCD camera was used not only to locate proper areas of ICs for the following up thermal imaging but also to photograph the ICs before and after been covered with R6G dyes.

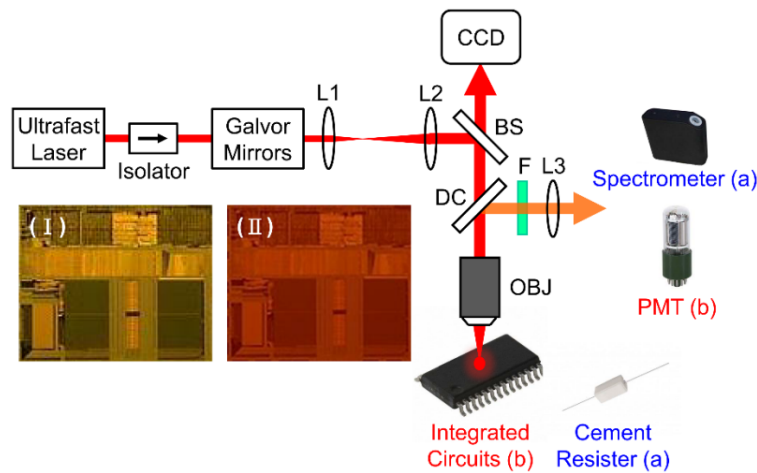


Fig. 1. Microscope setup for high-resolution thermal imaging. L1 and L2 are a pair of relay lenses for the raster scanning of laser beam; BS: beamsplitter; DC: dichroic beamsplitter; OBJ: objective lens; F: filter, KG5; L3: lens for TPF collection. The insets of Figs. 1 and 2 (obtained by CCD) are bright-field images of ICs before and after covering with a thin-film of fluorescent dye, respectively.

### 3. Thermal-Optical Properties of R6G and its calibration to temperature

Figure 2 presents the thermooptical properties of the R6G thin-films, as determined in Part (a) of the experiments. We employed the measured temperature-dependent TPF spectra as a database by which to transform TPF intensities into local temperatures within ICs. The physical mechanism underlying the temperature dependence of TPF intensity can be attributed to non-radiative de-excitation during the conversion process, which boosts the increase in temperature, thereby leading to a decrease in the TPF signal. In Fig. 2(a), the measured TPF emission spectra of R6G were all centered at 620 nm, regardless of temperature. As expected, the peak intensities decreased with an increase in temperature. Each curve at a specific temperature was integrated over all wavelengths to obtain the relationship between the temperature ( $T$ ) and total TPF intensity ( $I_{\text{TPF}}$ ) as plotted in the black circles in Fig. 2(b). In Fig. 2(b), we observed a linear relationship that was well-fitted using  $I_{\text{TPF}} = -0.067T + 8.029$ . The negative slope represents the thermooptical properties of R6G material and acts as a key parameter in the transformation of TPF intensities into localized temperature with high resolution from pixel to pixel.

In TPF thermal imaging, to demonstrate high-accuracy temperature measurements of ICs over the long-term, the photobleaching effect, which is a photochemical phenomenon of a fluorescent molecule under high power illumination, of R6G must be avoided [27] because this effect will make the R6G unable to fluoresce permanently. Figure 2(c) presents TPF images of R6G thin-films obtained under continuous femtosecond pulse illumination measured over a period of 3 min with a 0.4 fps and a  $200 \times 200\ \mu\text{m}^2$  FOV using the experimental layout shown in Part (b) of Fig. 1. The intensities of all pixels in each image were averaged to obtain the average TPF intensity, as shown by the solid line in Fig. 2(c). The

inset of Fig. 2(c) presents selected images at selected points in time (black arrows). Figure 2(c) shows a decrease of only 2% in the average TPF intensity over a period of 3 min, indicating that the photobleaching of R6G films can be disregarded.

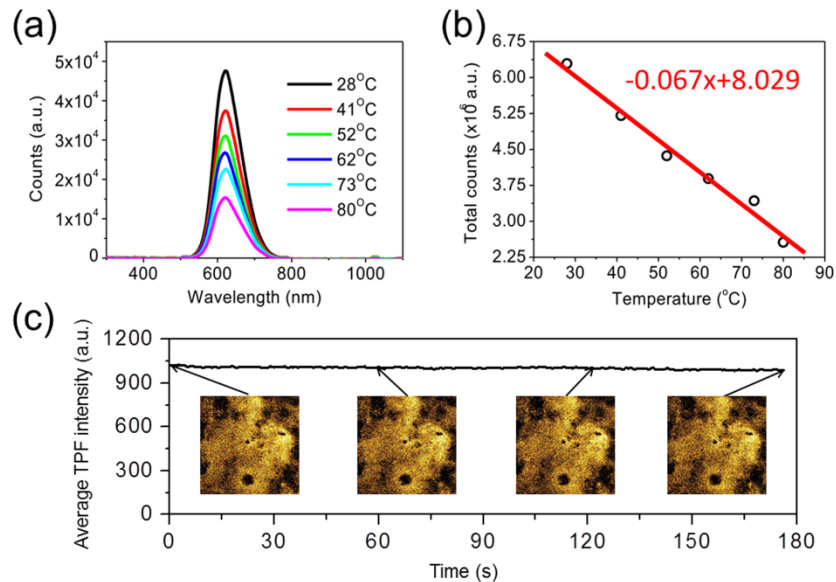


Fig. 2. (a) Thermal spectrum of R6G accounting for two-photon fluorescence (TPF) emissions at different temperatures. (b) Relationship of total TPF intensity to specific temperature, as derived from (a). The clear linear trend is used to determine local temperature values. (c) Verification of TPF photobleaching, which could influence the precision of local temperature values. The insets are TPF thermal images of R6G on the surface of a cement resistor at specific time points (black arrows). Following the calculation of average TPF intensity, we observed only a 2% decrease in intensity over a period of 3 min, demonstrating that the effects of photobleaching can be disregarded.

#### 4. Thermal Microscopy on ICs

Based on the measured thermo-optical properties of R6G material in Sec. 3, scheme (b) in Fig. 1 was used to obtain time-lapse thermal images of IC circuits. A series of thermal images was created from power-off to power-on over a period of 78 s with a  $\sim 2.6$  second time interval between each image. Figures 3(a) and 3(b) present selected TPF images at power-off (0 second) and power-on (78 second), respectively. In the thermal microscopic image of Fig. 3(c), the localized temperature specified with different colors is obtained by comparing the ratio of TPF intensity between the two TPF images (i.e. compared Fig. 3(a) with 3(b)), and using the  $-0.067$  negative thermo-optical slope in Fig. 2(b). The size of the images in Figs. 3(a)-3(c) was  $200\ \mu\text{m}$  by  $200\ \mu\text{m}$ . As shown in Fig. 3(c), after power-on for 78 sec, the temperatures over the metal tracks were higher than those in the surrounding areas. This indicates that the metal track structures tend to be heated more quickly than do the surrounding (non-metallic) areas.

Figure 3(d) shows the detailed flowchart for describing how Fig. 3(c) was taken and calculated. It is the general procedure followed to derive thermal images from TPF images in this work. The time-dependent temperature values in local areas are indicated by the black and blue rectangles in Fig. 3(c) and the solid squares and solid circles in Fig. 3(e), respectively. The formula used in data analysis was  $y = b \cdot \exp(-t/t_c) + T_e$ , where  $b$  is a proportional constant;  $t_c$  is the time required to reach thermal equilibrium; and  $T_e$  is the equilibrium temperature. After data fitting, the black curve is analogous to a normal heat-transfer function, from which the local temperature is saturated toward an equilibrium temperature ( $T_e = 30.9\ \text{°C}$ ;  $t_c = 36\ \text{s}$ ). In contrast, the blue curve continues rising after 36 s ( $t_c$

= 70 s), which indicates that the position of the blue rectangle is more far away from the heat source than is the black rectangle. In contrast, the area within the blue rectangle tends to be heated more quickly and easily ( $T_e = 33.9\text{ }^\circ\text{C}$ ), which may be indicative of a thermally induced defect. In addition, the respective black-dotted and blue-dotted curves in Fig. 3(e) illustrate the temperature difference with respect to time evolution within the areas of black and blue rectangles in Fig. 3(c). The spatial resolution of the thermal image is approximately 850 nm, which was analyzed from the fine structures of ICs in TPF images.

The precision of the temperature values was calculated from the intensity fluctuations in the TPF images onto the IC surface at constant temperature. Figure 3 (f) shows the TPF images when the IC chip was power-off as the surface at constant temperature. The percentage of intensity fluctuation was 10/256, corresponding to a 3.9% intensity noise. The temperature resolution can be calculated as the 3.9% intensity noise divided by the 0.067 thermooptical slope of R6G materials. The temperature resolution was calculated to be 0.58  $^\circ\text{C}$ , which is in line with typical thermal detectors with sub-degree temperature resolution.

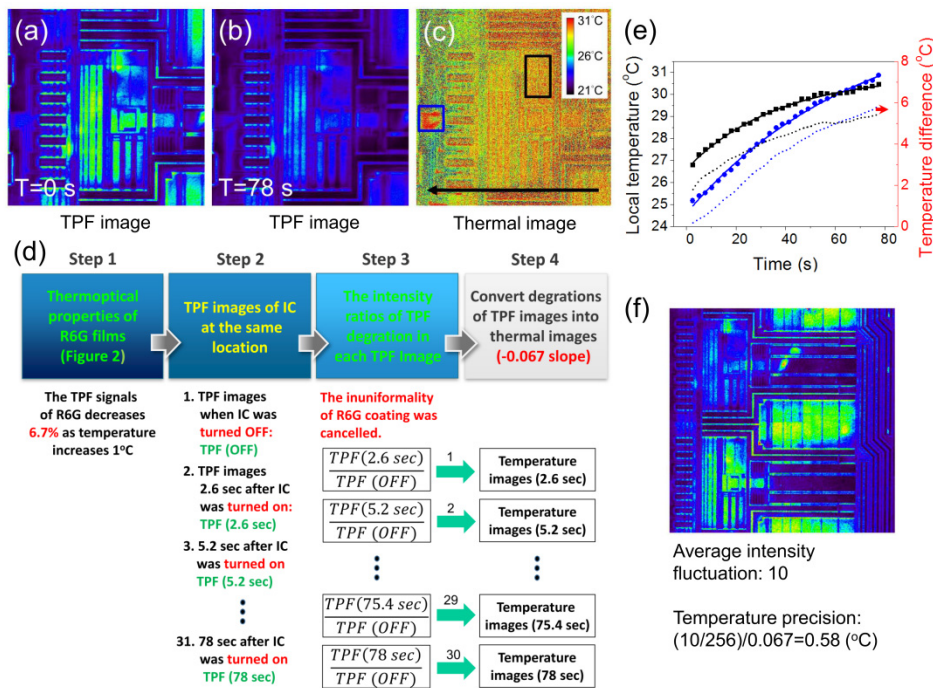


Fig. 3. (a) and (b) show TPF images of IC circuitry at time zero and 78 s, respectively. (c) Thermal image which is calculated from (a) and (b) and registered by a color map for different temperatures. The areas within the black and blue rectangles will be analyzed to illustrate how temperature increases with time in Fig. 3(e). The black arrow indicates the direction of heat flow after power-on. (d) A detailed flowchart for describing how Fig. 3(c) is taken. It is the general procedure followed to derive thermal images in this work. (e) elucidates the dependency of temperature on time, as analyzed by an exponential function. Moreover, the temperature difference with respect to time evolution is provided. (f) TPF image series from ICs without applied voltage. The average intensity fluctuations were measured in more than ten areas and the value is 10. Compared with the intensity depth (256) and the value of the negative slope (0.067), we calculated the temperature precision at 0.58. Image size of (a)-(c) is 200 x 200  $\mu\text{m}^2$ , while the image size of (e) is 590 x 590  $\mu\text{m}^2$ .

The proposed approach to IC thermal inspection was applied to the imaging of various types of IC, as indicated by the rows of matrix images in Fig. 4. In this part of the experiments, thermal anomalies were observed in the metal tracks under operation. Using the thermal-gradient method in Fig. 3, we were able to estimate the precise locations in which

thermal-induced defects were most likely to develop. The images in Fig. 4 show zoomed in areas of ICs, clearly indicating the physical structure of the metal tracks.

In the matrix image in Fig. 4, the first column shows IC images before turning on the power. It is impossible to predict hotspots when using only the initial TPF images from the first column or TPF images obtained at any one time throughout the evolution of the process. The second column of Fig. 4 shows the variations in TPF signal between power-off and power-on (a 2-s duration) in various circuit structures. The small temperature variations indicate that this length of time was insufficient for the generation and propagation of heat.

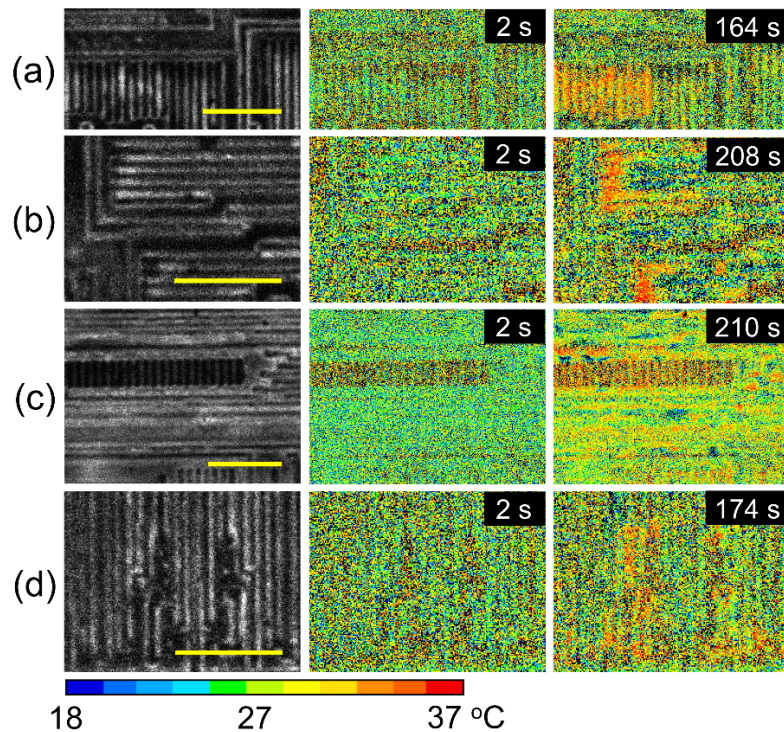


Fig. 4. Zoomed in images of (a) typical metal tracks, (b) metal tracks at the bend, (c) thin metal tracks, and (d) damaged tracks on ICs. The columns from left to right are TPF intensity images, thermal images at power-on for 2 s, and thermal images at power-on for more than 2 min, respectively. Thermal images are color-coded with a color bar below, which was calculated based on the relationship between TPF intensity and local temperature. Scale bar: 10  $\mu\text{m}$ .

As shown in the third column in Fig. 4, the thermal images show hotspots after the power was on for over 2 min. In Fig. 4(a), some areas have a higher temperature (as indicated by the orange-red color) than do their surrounding areas, regardless of similarities in the structure of the metal tracks. In Fig. 4(b), the metal tracks at the bend exhibit high temperatures, which can be ascribed to the high local density of electrons in the tracks. This hotspot may in turn influence the performance of ICs. In Fig. 4(c), higher temperature was achieved in the thinner metal lines. This was expected due to their high resistance values. Figure 4(d) shows some damaged metal tracks following excavation of the ICs. The shorted and/or open circuits in these locations presented higher temperatures than did the surrounding areas. The results of TPF thermal imaging indicate that hotspots are likely to appear in the following types of structures: thinner tracks, bends, and the damaged/deformed structures. As indicated in Fig. 4, the proposed scheme is able to identify possible hotspots or defects even among similar circuit structures.



## 5. Discussions, Conclusions and Future Perspective

In this work, we proposed a rapid, non-contact approach to the thermal microscopy on ICs with sub- $\mu\text{m}$  spatial resolution and sub-degree temperature resolution. The imaging speed (0.4 fps) is fast enough to analyze the microscopic thermal dynamics when the IC chip is power-on. The imaging speed can of course scale up to thousands of fps by current state-of-art TPF microscopy [28].

Although there may be some waste heat during the TPF process (16.9% of absorbed energy), with only a 20 mW illumination power onto the ICs, there was a maximum 3.4 mW of generated heat distributed within the whole FOV. From the experimental result of Fig. 2(c), the intensity of TPF remains nearly constant, this means that neither photobleaching of R6G nor wasted heat from laser illumination appeared in our experiments.

Moreover, the  $0.58^\circ\text{C}$  temperature precision was calculated with the imaging parameters of 20 mW average power onto the ICs, 0.9-NA microscope objective, and the frame time of 2.6 second. This temperature precision can be further improved by reducing the percentage of intensity fluctuations or replace the TPF-active material with a larger thermooptical slope. The percentage of intensity fluctuations in the TPF images can be easily reduced by increasing the image integration time. Therefore, there is a compromise between the temperature resolution and imaging acquisition speed.

In experiments, a compact 1030-nm laser with a turn-key operation was used. Only 20 mW average power was required to perform thermal imaging without any side effects, such as photobleaching or photothermal effect under continuous laser illumination, as shown in Fig. 2(c). In the future, low-cost and stable Ytterbium-doped fiber laser could be a suitable candidate in industrial applications, not only for research use [29]. On the other hand, for R6G material, TPF absorption cross-section at 800 nm is higher than that at 1030 nm [30]. Therefore, with an 800-nm laser pumping, less laser dose is required to perform TPF, as compared with 1030-nm laser pumping. However, the R6G thin-film is sufficiently sensitive to 1030-nm laser wavelength because the TPF signal is easily detected without the side effect mentioned above, as shown in Fig. 2(c).

In our preliminary demonstrations, spin-coating with thermooptical materials onto ICs may cause our approach not perfectly non-invasive and induce potential damage to the ICs. As shown in Fig. 5(a), this issue can be addressed by utilizing a fiber-optic packaged TPF probe, whose experimental arrangement and working principle were similar to those utilized in nonlinear fiber-optic TPF endoscopes [31–34]. This fiber-optic packaged TPF probe was composed of a fiber-delivered input, a 2D scanner, a pair of relay lenses, a dichroic mirror (DM), an objective lens (OBJ), a thin-film coating R6G, as a portable thermooptical sensor, and a multimode fiber to collect the TPF signals. In the dashed green-box of Fig. 5(a), the output of the collimated beam from the fiber laser was connected to the input end of TPF probe. With a 2D scanner, the laser beams were sequentially scanned over a plane. Through a pair of relay lens ( $L_1$  and  $L_2$ ) with a 4-f configuration and an OBJ, laser beams were sequentially scanned within the focal plane. In this proposal, the R6G thin-film sensor was placed on the focal plane and the ratio of TPF signals of individual locations represent the localized temperatures (i.e., the same concept in Section 4). The generated TPF signals will be collected through the same OBJ, extracted with a DM, and then focused onto a multimode fiber connected to a photomultiplier tube (PMT) by another focusing lens ( $L_3$ ). All components in the dashed-green box of Fig. 5(a) can be packaged together as a translational probe. The probe can be quite close to the ICs to sense the localized temperature of IC surface. Thus, the process of spin-coating with R6G is avoided and this improved version is non-invasive and less harmful to ICs.

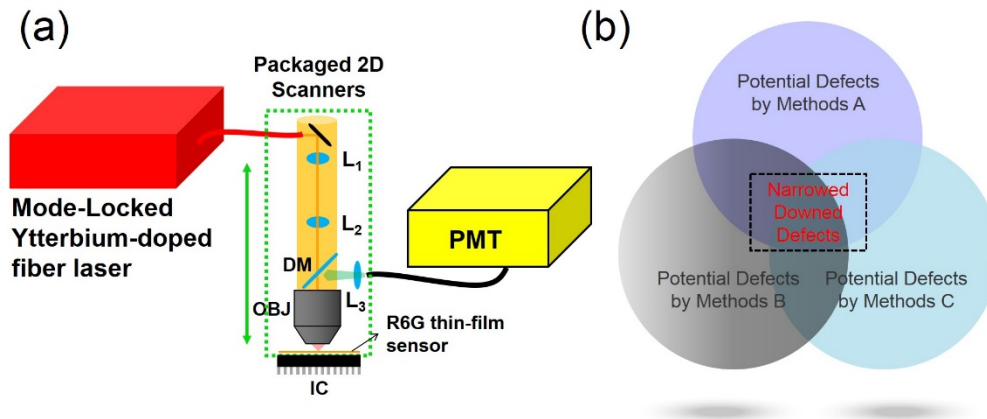


Fig. 5. (a) The schematics of a fiber-optic packaged TPF probe (in green-dashed box) to avoid the step of spin-coating with fluorescent dyes. The probe can be very close to the ICs when obtaining the thermal microscopic images. The proposed scheme allows the TPF probe to be minimal invasive and less harmful to ICs. DM: dichroic mirror; OBJ: objective lens; and PMT: photomultiplier tube. (b) The schematics of multimodal weak point inspection, method A to methods C, to increase the diagnosis precision of determining potential defects.

In this work, the proposed TPF thermal microscope can be utilized to monitor the localized hotspots, which may be potential weak points or defects, as shown in the blue box in Fig. 3(c) and the positions with a higher temperature in Fig. 4. The ranges of potential weak points or defects can be further narrowed down by the other IC defect diagnosis methods. As shown in Fig. 5(b), performing multimodal defect diagnosis is helpful to reduce the errors in determining the potential weak points or defects. Of course, in the multimodal defect diagnosis, there will be a compromise between the time/cost and accuracy in weak point diagnosis. How to find the exact and optimized combinations of methods A, B, and C shown in Fig. 5(b) is still an interesting research topic in the future. On the other hand, it is additionally helpful to economize the time required for measurements by multimodal detection. For example, one can pre-screen the whole IC with a MIR camera with a larger FOV to locate the areas of potential defects or possible weak points. These areas can be further analyzed with a higher spatial resolution by our proposed TPF thermal microscope.

In conclusion, this work reports on an advanced IC thermal-imaging method, which uses R6G thin-film as a fluorescent-thermal contrast agent. The proposed scheme enables sub-micron spatial resolution, temporal resolution of several seconds, and sub-degree temperature resolution, which is sufficient to locate hotspots in ICs. In experiments, R6G was spin-coated on the surface of ICs for use as a transformer to convert localized temperature into variations in fluorescence intensity on images. A calibration curve is then formulated to represent the thermooptical properties of R6G. This system enables the dynamic observation of the generation, propagation, and diffusion of heat in a high spatially precise and non-contact manner.

Our results show that some circuit structures are heated up more easily, including bent lines, thin lines, and damaged lines. In the future, materials with a larger absolute magnitude of slope could be used to enhance the temperature sensitivity of the thermal microscope. Other types of circuit could also be imaged prior to mass production to enable *in situ* monitoring of potential weak points.

## Funding

Ministry of Science and Technology of Taiwan (104-2221-E-009-155-MY3, 105-2112-M-110-015-MY2); Department of Medical Research of Chi-Mei Medical Center, Tainan, Taiwan.

**Acknowledgments**

The authors thank Prof. Fu-Jen Kao at National Yang-Ming University, Taiwan for loaning useful equipment. The authors also thank Prof. Wallace Lin of National Cheng-Kung University, Taiwan for fruitful discussions.